Asian Journal of Physics (AJP) (2008) **00**, 000–000

New Aspects on Particle Acceleration in Solar Flares from RHESSI Observations

Markus J. Aschwanden*
Lockheed Martin Advanced Technology Center,
Solar and Astrophysics Laboratory, Bldg. 252, Org. ADBS,
3251 Hanover St., Palo Alto, CA 94304, USA

Received 2008 May 16; accepted 2008 ...

Abstract. In this review we highlight a number of recent RHESSI observations that are directly relevant to the study of particle acceleration processes in solar flares. Many observations confirm our basic standard models of acceleration in various types of coronal magnetic reconnection regions, but reveal a number of unexpected features that either require more detailed magnetic, hydrodynamic, and kinetic modeling or rethinking in terms of alternative models.

Key words: solar flares – particle acceleration – hard X-rays

1. Introduction

The fundamental problem of particle acceleration in solar flares we try to study can only be approached by remote-sensing. Primary diagnostics is provided by bremsstrahlung, gyrosynchrotron emission, and plasma emission excited by non-thermal electrons in hard X-rays and radio wavelengths, as well as by free-free bremsstrahlung in soft X-rays. These are all secondary processes after the particles have already been accelerated, while a direct primary diagnostic of the acceleration process is not accessible. Although we gathered overwhelming evidence that particle acceleration occurs in magnetic reconnection processes and shock waves generated in flares and coronal mass ejections (CMEs), we are not able to directly measure the accelerating electromagnetic fields, and thus have to reconstruct the physics of the acceleration process indirectly by modeling the magnetic configurations and by taking the propagation kinematics and energy loss targets of the accelerated particles into account. In this review we highlight a number of recent observations with the *Ramaty High Energy Solar Spectrosocpy Imager (RHESSI)* (Lin et al. 2002) that provide new evidence for existing models or challenge previous concepts of our view of particle acceleration processes in solar flares.

*e-mail:aschwanden@lmsal.com

The subject of particle acceleration in solar flares has been systematically described in recent monographs and textbooks (Benz 1993, 2002; Aschwanden 2002, 2004, 2005; and references therein). More updated overviews can be found in Dennis et al. (2007), Benz (2008), and in a Special Topical Issue of *Space Science Reviews* on RHESSI results (eds. Lin, Emslie, Dennis, & Hudson) to be published in 2008, including a chapter focusing on particle acceleration (Holman et al. 2008).

2. Theoretical Aspects

2.1 *Particle Acceleration Mechanisms in Solar Flares*

Particle acceleration in solar flares is mostly explored by theoretical models, because neither macroscopic nor microscopic electric fields are directly measurable by remote-sensing methods. The motion of particles can be described in terms of acceleration by parallel electric fields, drift velocities caused by perpendicular forces (i.e., $E \times B$-drifts), and gyromotion caused by the Lorentz force of the magnetic field. Theoretical models of particle acceleration in solar flares can be broken down into three groups: (1) DC electric field acceleration, (2) stochastic or second-order Fermi acceleration, and (3) shock acceleration (for an overview see Table 1; for references see (Aschwanden 2004, p.470). In the models of the first group, there is a paradigm shift from large-scale DC electric fields (of the size of flare loops) to small-scale electric fields (of the size of magnetic islands produced by the tearing mode instability). The acceleration and trajectories of particles is studied more realistically in the inhomogeneous and time-varying electromagnetic fields around magnetic X-points and O-points of magnetic reconnection sites, rather than in static, homogeneous, large-scale Parker-type current sheets. The second group of models entails stochastic acceleration by gyroresonant wave-particle interactions, which can be driven by a variety of electrostatic and electromagnetic waves, supposed that wave turbulence is present at a sufficiently enhanced level and that the MHD turbulence cascading process is at work. The third group of acceleration models includes a rich variety of shock acceleration models, which is extensively explored in magnetospheric physics and could cross-fertilize solar flare models. Two major groups of models are studied in the context of solar flares (i.e., first-order Fermi acceleration or shock-drift acceleration, and diffusive shock acceleration).

Recently, shock acceleration has also been applied to the outflow regions of coronal magnetic reconnection sites, where first-order Fermi acceleration at the standing fast shock is a leading candidate. Traditionally, evidence for shock acceleration in solar flares came mainly from radio type II bursts. New trends in this area are the distinction of different acceleration sites that produce type II emission: flare blast waves, the leading edge of CMEs (bowshock), and shocks in internal and lateral parts of CMEs. In summary we can say that (1) all three basic acceleration mechanisms seem to play a role to a variable degree in some parts of solar flares and CMEs, (2) the distinction between the three basic models becomes more

Acceleration Mechanisms	Electromagnetic fields
DC electric field acceleration:	
– Sub-Dreicer fields, runaway acceleration	$E < E_D$
– Super-Dreicer fields	$E > E_D$
– Current sheet (X-point) collapse	$E = -u_{inflow} \times B$
– Magnetic island (O-point) coalescence	$E_{conv} = -u_{coal} \times B$
– (Filamentary current sheet: X- and O-points)	
– Double layers	$E = -\nabla V$
– Betatron acceleration (magnetic pumping)	$\nabla \times E = -(1/c)(dB/dt)$
Stochastic (or second-order Fermi) acceleration:	
Gyroresonant wave-particle interactions with:	
– whistler (R-) and L-waves	$k \parallel B$
– O- and X-waves	$k \perp B$
– Alfvén waves (transit time damping)	$k \parallel B$
– Magneto-acoustic waves	$k \perp B$
– Langmuir waves	$k \parallel B$
– Lower hybrid waves	$k \perp B$
Shock acceleration:	
Shock-drift (or first-order Fermi) acceleration	
– Fast shocks in reconnection outflow	
– Mirror-trap in reconnection outflow	
Diffusive-shock acceleration	

Table 1. Overview of particle acceleration mechanisms in solar flares (Aschwanden 2004).

blurred in the more realistic (stochastic) models, and (3) the relative importance and efficiency of various acceleration models can only be assessed by including a realistic description of the electromagnetic fields, kinetic particle distributions, and MHD evolution of magnetic reconnection regions pertinent to solar flares.

Particle acceleration and propagation, however, generally cannot easily be separated from each other in solar flares, as long as we cannot localize and pin down the extent of the accelerating fields within the geometry of the reconnection regions, wave turbulence regions, or shock regions. Particle kinematics, the quantitative analysis of particle trajectories, has been systematically explored in solar flares by performing high-precision energy-dependent time delay measurements with the large-area detectors of the *Compton Gamma-Ray Observatory (CGRO)*. There are essentially five different kinematic processes that play a role in the timing of nonthermal particles energized during flares: (1) acceleration, (2) injection, (3) free-streaming propagation, (4) magnetic trapping, and (5) precipitation and energy loss. The time structures of hard X-ray and radio emission from nonthermal particles indicate that the observed energy-dependent timing is dominated either by free-streaming propagation (obeying the expected electron time-of-flight disper-

sion) or by magnetic trapping in the weak-diffusion limit (where the trapping times are controlled by collisional pitch angle scattering). The measurement of the velocity dispersion from energy-dependent hard X-ray delays allows then to localize the acceleration region, which was invariably found in the cusp of postflare loops.

2.2 *Magnetic Topology of Acceleration Region*

The physical understanding of particle acceleration processes that occur in magnetic reconnection regions of solar flares requires detailed geometric models of their magnetic topology. There are three basic topologies of magnetic reconnection geometries between open and closed field lines: The pre-reconnection geometry consists of a pair of (1) open-open, (2) open-closed, or (3) closed-closed magnetic field lines (Fig. 1). If these pairs of pre-reconnection magnetic field lines are coplanar, we have a 2D model, as shown in Fig. 1 (top row, thick dashed lines). The disjoint field lines are brought into contact with each other during the reconnection process (dotted lines in Fig. 1, top row), and then relax into the post-reconnection configuration (shown with solid double lines in Fig. 1 top row).

A standard 2D flare model of the dipolar or open-open type is the Carmichael-Sturrock-Hirayama-Kopp-Pneuman (CSHKP) reconnection model. It starts with a helmet-streamer configuration with two antiparallel magnetic field lines above the cusp of the streamer, where a Y-type reconnection geometry occurs in the cusp, as observed in the famous "candle-flame" flare of 1992-Feb-21 (Tsuneta et al. 1992), which is similar to the 1999-Mar-18 flare shown in Fig. 1 (bottom left). We see that the end product is one closed (postflare) loop (Fig. 1, top left). The observations (Fig. 1, bottom left) show only the lower part with a cusp and postflare loop, but in a vertically symmetric X-type geometry we would expect also an upward reconnected segment that escapes into interplanetary space.

The tripolar type involves three magnetic poles (Fig. 1, top middle), where magnetic reconnection is referred to as *"interchange reconnection"*. Variants of this type of magnetic reconnection in tripolar geometries were also envisioned in the context of emerging-flux models (Heyvaerts et al. 1977) and particularly after the discovery of soft X-ray plasma jets with Yohkoh (Shibata et al. 1992). The observation of long straight soft X-ray jets (e.g., Fig. 1, bottom middle) were taken as evidence of plasma flows along open field lines, a fact that constitutes a flare-like process between a closed and an open field line. The end product of tripolar (open-closed) reconnection is one closed post-reconnection (postflare) loop and one open field line (Fig. 1, top middle), usually associated with a soft X-ray jet.

The quadrupolar type (Fig. 1, top right) is also called interacting-loop model and has been theoretically modeled in terms of magnetic flux transfer between two current-carrying loops (Melrose 1997). Classical examples have been observed with Yohkoh/SXT by Hanaoka (1996), Nishio et al. (1997), and modeled in terms of 3D quadrupolar geometries by Aschwanden et al. (1999). The initial situation as well as the end product of quadrupolar reconnection are two closed loops, but the footpoint connectivities between opposite polarities are switched during reconnec-

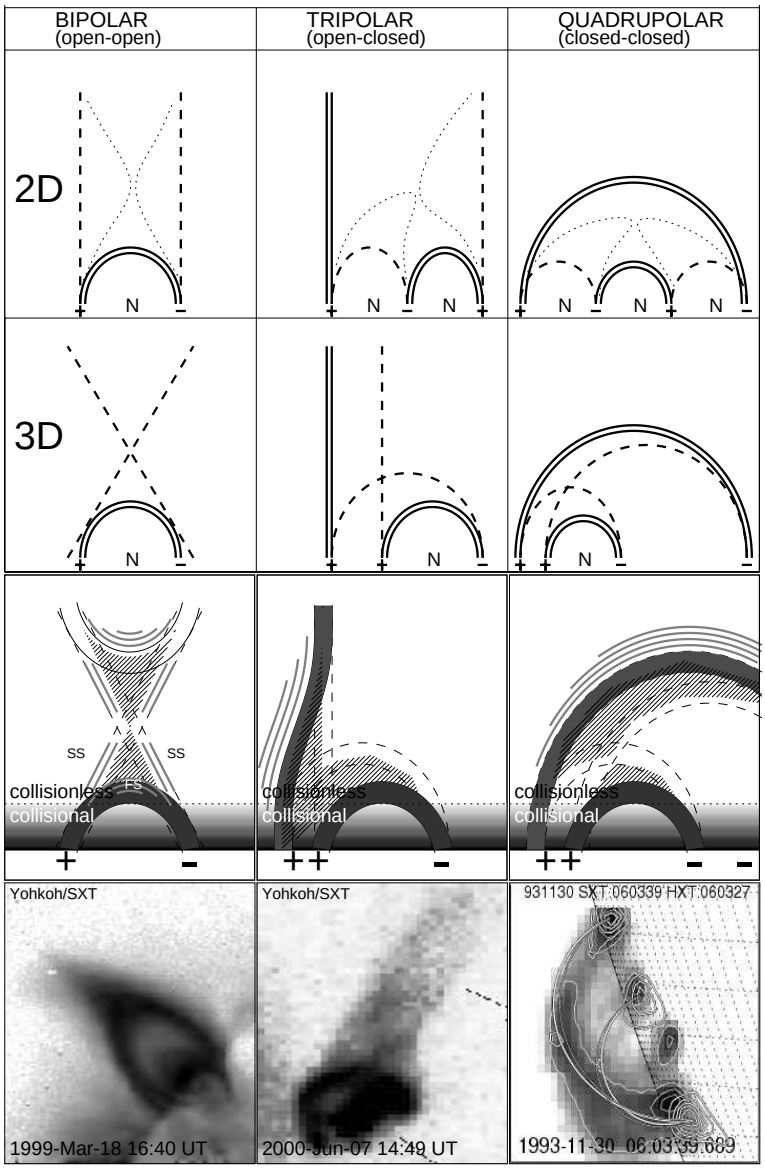

Figure 1. The topology of magnetic reconnection regions is classified into three combinations: bipolar or open-open (left column), tripolar or open-closed (middle column), and quadrupolar or closed-closed field line reconnection (right column). The 2D versions are shown in the top row, with the pre-reconnection field lines marked with dashed lines, during reconnection with dotted lines, and post-reconnection field lines with double solid linestyle. The 3D versions are indicated in the second row, where the pre-reconnection field lines are not coplanar, but located behind each other. The third row indicates the acceleration regions (hatched), the relative densities (greyscale), and upward/sideward directed shocks (grey lines). The bottom row shows flare observations from Yohkoh/SXT that correspond to the three different reconnection topologies (Aschwanden 2002, 2005).

tion. The outcomes are similar in 2D and 3D (Fig. 1, second row), except that the footpoints and loops are not lined up in a single plane in 3D, but can have arbitrary shear angles between the pre-reconnection loops.

Observations usually do not make the pre-reconnection configuration visible, but display the post-reconnection field lines only, because they become filled with dense hot flare plasma by the chromospheric evaporation process, which is easily to detect in soft X-rays, as shown in the examples in Fig. 1 (bottom row). Most solar flare observations are interpreted in terms of one of these basic magnetic topologies, which provide us the approximate location and geometry of particle acceleration regions (hatched areas in 3rd row of Fig. 1) and the likely propagation paths of accelerated electrons along the outgoing magnetic field lines.

3. New Aspects from RHESSI Observations

In recent years (since 2002) RHESSI observations provide us the most exciting and powerful data in the study of acceleration processes of high-energy particles in solar flares. RHESSI observations revealed a number of unexpected clues and surprised us also with dazzling new findings that challenge previously established concepts and models. In the following we review a number of highlights, new insights, and controversies from RHESSI observations.

3.1 *Hard X-Ray Evidence for Bipolar X-Point Reconnection*

The standard (Carmichael-Sturrock-Hirayama-Kopp-Pneuman) flare model envisions two oppositely directed magnetic field regions that are stretched in the vertical direction to form a current sheet where they reconnect. After reconnection, the newly-connected field lines form a cusp beneath the X-type reconnection point and relax into a semi-circular, dipolar post-flare loop, which has two conjugate footpoints where the nonthermal hard X-ray emission originates. In a recent unique RHESSI observation (Sui & Holman 2003), two coronal hard X-ray sources were observed, symmetrically placed below and above the putative X-point, at locations where the downward and upward outflows from the reconnection region are expected (Fig. 2). Moreover, the separation of the sources increased with lower energies in the thermal range of $\approx 10 - 16$ keV. Since increasing temperatures affect higher photon energies, this particular configuration indicates that thermal hard X-ray emission is observed hottest near the X-point, and progressively cooler with increasing distance from the X-point. This result was interpreted in terms of a current sheet formed above the flare loop location, as expected in the standard flare model. This observation can be considered as the first direct localization of a current sheet in a flare, and thus provides strong support for the standard model.

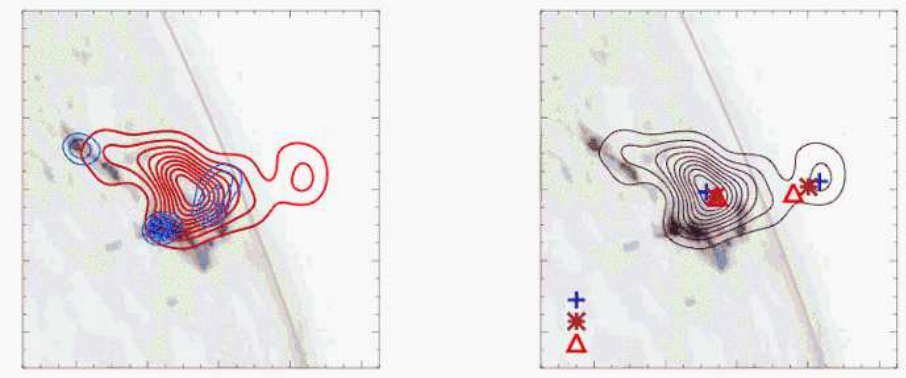

Figure 2. *Left: TRACE 1600 Å image of the 2002 April 15, 23:11 UT, flare, overlaid with RHESSI contours of thermal and nonthermal emission. Right: Same image with contours of RHESSI 10-15 keV emission. The symbols indicate the centroid of the coronal sources in the energy bands of 6-8 keV, 10-12 keV, and 16-20 keV for the lower coronal source, and 10-12 keV, 12-14 keV, and 14-16 keV for the upper coronal source. Note the increasing separation of the coronal hard X-ray sources towards lower thermal energies (Sui & Holman 2003).*

3.2 *Hard X-ray Evidence for Tripolar Magnetic Reconnection*

There is a class of magnetic topologies that involve reconnection between an open field line and a closed field line, which in the simplest case corresponds to a "tripolar" configuration. After reconnection, one footpoint of the closed loop becomes the footpoint of the open field line. In more complex 3D topologies, an isolated polarity is surrounded by a region of opposite polarity, which creates a coronal nullpoint at the intersection of the separatrix dome and the vertical spine field line (Fig. 3 top). Flares that are consistent with such tripolar topologies (in a 2D plane) have been observed with TRACE (Fletcher et al. 2001) and with RHESSI (Krucker & Hudson 2004). A by-product of such tripolar flares is the appearance of linear jets that are detectable in soft X-rays and EUV, as well as escaping electron beams that produce radio type III bursts (Fig. 3 bottom).

3.3 *Displaced Electron and Ion Acceleration Sources*

The thick-target model assumes that nonthermal particles precipitate to the chromosphere and produce collisional bremsstrahlung there, so we expect that the hard X-ray footpoint sources are more or less cospatial at all high energies, except for a possible difference in chromospheric altitude. If ions are accelerated in the same source as the electrons, we expect also the gamma-ray emission resulting from nuclear de-excitation lines to be cospatial with the hard X-rays. It was therefore a big surprise that RHESSI observations for the first time revealed disparate footpoint sources for hard X-rays and 2.223 MeV gamma rays (Fig. 4), which is produced

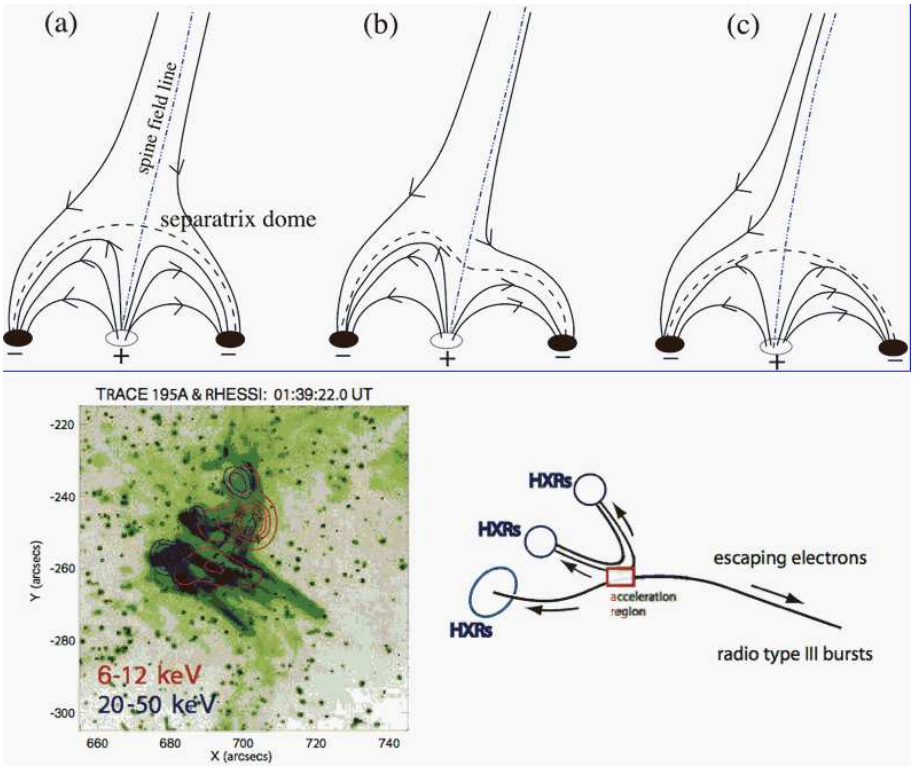

Figure 3. *Top: Magnetic topology inferred for the 1993 May 3, 23:05 UT, flare, suggesting reconnection at a 3D nullpoint where the spine field line intersects the separatrix dome (Fletcher et al. 2001) Bottom: A similar topology is observed in a flare observed with RHESSI and TRACE (Krucker & Hudson 2004).*

by the capture of neutrons, produced by accelerated protons and heavier nuclei (C, N, O, Fe). A displacement of $\approx 20''$was observed during the 2002 July 23, 00:30 UT, flare (Lin et al. 2003a; Hurford et al. 2003). Similar displacements were also observed in other flares, as illustrated in Fig. 4 (Hurford et al. 2006).

This came as a surprise and challenges us to think of either different acceleration mechanisms or different propagation trajectories for electrons and ions. Theoretical interpretation attempts range from separate acceleration sources in flare reconnection sites and CME shocks (Vestrand & Forrest 1993), different acceleration path lengths for electrons and ions in the stochastic acceleration process (Emslie et al. 2004), displacements due to gradient and curvature drift of the electrons and ions in opposite directions along the flare magnetic arcade (Hurford et al. 2006), to charge separation in the super-Dreicer electric field in a reconnecting non-neutral current sheet (Zharkova & Gordovskyy 2004). There is still no consensus about the most likely interpretation.

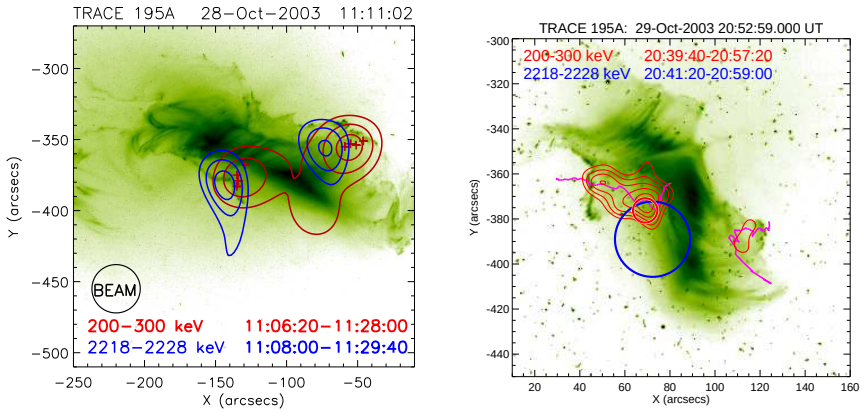

Figure 4. *RHESSI images (contours) overlaid on TRACE images are shown for the two flares of 2003 Oct 28, 11:06 UT (left) and 2002 Oct 29, 20:40 UT (right). Note the displacement between the 200-300 keV hard X-ray emission and the 2.2 MeV neutron-capture gamma-ray line emission (Hurford et al. 2006).*

3.4 *Hard X-ray Emission Along Double Ribbons*

The classical CSHKP model predicts two ribbons of opposite magnetic polarity on both sides of the neutral line, which are expected to coincide with the locations of non-thermal thick-target bremsstrahlung at the footpoints of flare loops, if our model of loop-top acceleration is correct. However, such ribbons are rarely seen in hard X-rays, either due to insufficient dynamic range in the hard X-ray imaging method, or, more interestingly, due to a failure or our simple-minded application of the thick-target bremsstrahlung model. Measuring the magnetic field strength along H-α flare ribbons, Asai et al. (2002) found that the magnetic field strength in H-α kernels accompanied by hard X-ray radiation (observed with Yohkoh/HXT) is about three times larger than in those without hard X-rays. However, RHESSI observations revealed in some flares complete hard X-ray-illuminated flare ribbons (Liu et al. 2007a, 2007b, 2008; Jing et al. 2007), best seen in the 25-60 keV energy band (Fig. 5).

In the *runaway tether-cutting model* (Fig. 6) proposed by Moore et al. (2001), the footpoint-to-ribbon transformation of the hard X-ray source is a natural outcome of the sigmoid-to-arcade evolution of the magnetic field configuration (Liu et al. 2007b). However, since such complete ribbons are rarely detected even with RHESSI, it is still not clear whether the detection of complete hard X-ray ribbons is related to the spatial uniformity of the energy release rate (or acceleration region), the spatial distribution of the magnetic field strength (which may be related to the accelerating electromagnetic fields), or to the dynamic range of the imaging algorithm.

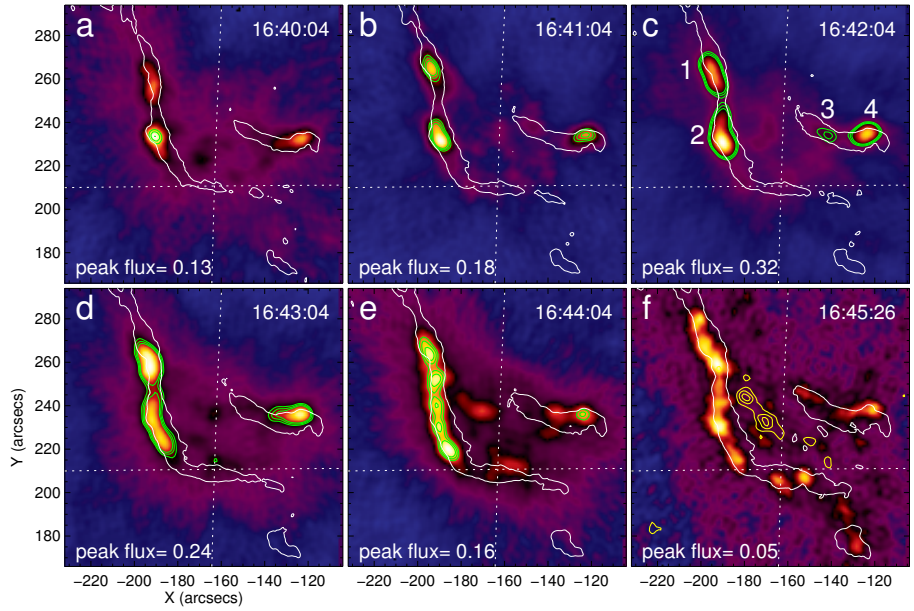

Figure 5. *Top: A sequence of RHESSI 25-60 keV images during the flare of 2005 May 13, 16:36 UT, overlaid on a TRACE 1600 Å image. Note that the hard X-ray ribbons (white areas) outline most of the UV ribbons (contours), (Liu et al. 2007b).*

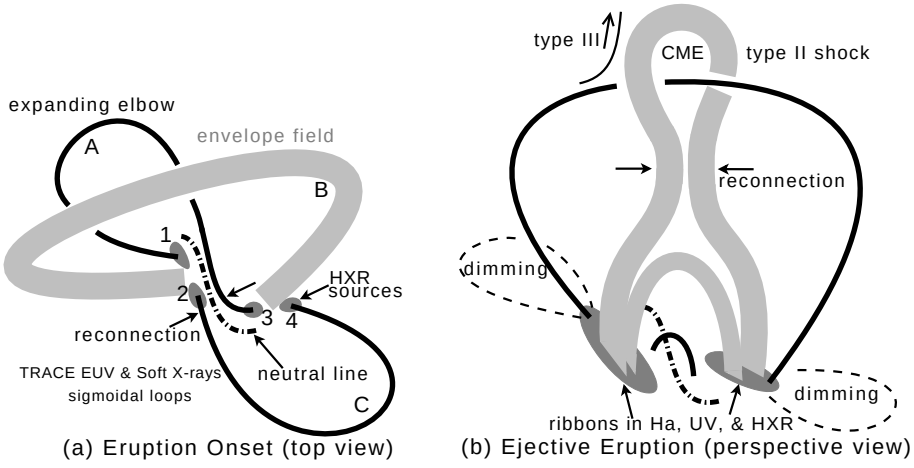

Figure 6. *Sketch of the "runaway tether-cutting mode" of Moore et al. (2001), showing the evolution of an initial sigmoid magnetic configuration with point-like hard X-ray kernels at the eruption onset (left) to an arcade-like post-reconnection configuration with double-ribbon hard X-ray sources (right), (Liu et al. 2007b).*

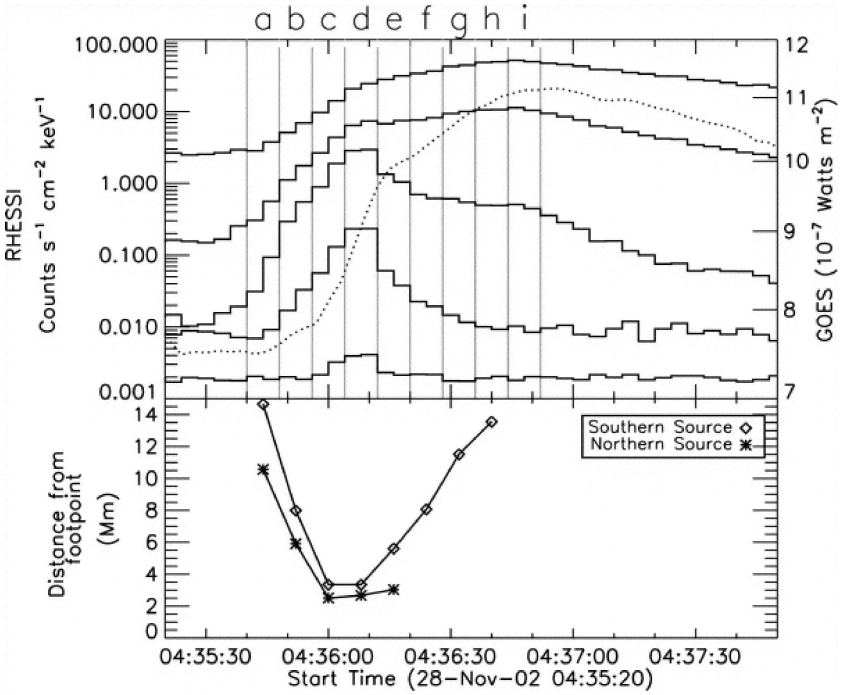

Figure 7. *RHESSI 3-6, 6-12, 12-25, and 50-100 keV (solid lines) and GOES 1-8 Å (dotted curve) light curves of the 2002 Nov 28, 04:35 UT, flare (top), along with the evolution of the altitude of the centroid of the RHESSI hard X-ray source, with respect to the footpoint baseline (bottom). Note the initial downward and subsequent upward motion (Sui et al. 2006).*

3.5 *Downward-Upward Motion of Hard X-Ray Source*

Another discovery of RHESSI observations is an intriguing motion of hard X-ray sources during the flare evolution. In the 2002 Nov 28, 04:35 UT, flare, for instance, hard X-ray sources at energies of 3-10 keV move from an initial altitude of $\approx 15,000$ km at the beginning of the flare first down to ≈ 3000 km during the rise time (≈ 30 s), and move subsequently upward again, reaching their original altitude during the decay time (≈ 60 s after flare onset), as shown in Figs. 7 and 8 (Sui et al. 2006).

While the upward motion can easily be understood in terms of the chromospheric evaporation model (Liu et al. 2006), which fills up the flare loops, increases their electron density, and thus rises the altitude of the thick-target energy loss region of 3-10 keV electrons (Aschwanden et al. 2002), the interpretation of the initial downward motion is much more challenging. Interpretations deal with the soft-hard-soft spectral evolution and low-energy cutoff of the injected electron distribution function (Sui et al. 2006). Alternatively, one could also imagine that the ratio of trapped to precipitating electrons in the cusp region where elec-

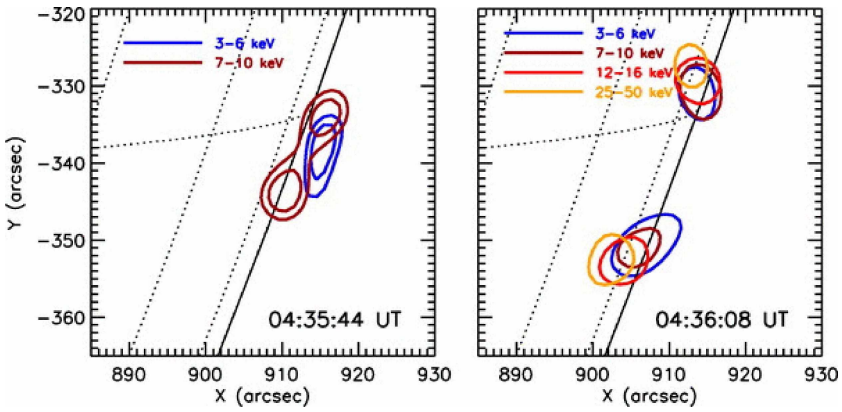

Figure 8. *RHESSI images in multiple energy bands at the beginning of the flare (left) and near the peak time of the flare (right). Note the downward motion during this time interval and the energy dependence with height (Sui et al. 2006).*

tron acceleration takes place is initially higher for low-energy electrons, and thus the initial downward motion could reflect a gradual transition from trap-dominated to precipitation-dominated nonthermal 3-10 keV bremsstrahlung emission. A dynamic model of a collapsing trap in the cusp region was modeled to explain both the initial downward motion and subsequent upward motion of the hard X-ray loop top source (Karlicky et al. 2006).

3.6 *Footpoint Motion and Reconnection Rate*

The footpoint motion of hard X-ray sources or flare ribbons reveals the evolution and progression of coronal magnetic reconnection sites, because there is a direct magnetic mapping from the reconnecting X-points to the footpoints due to the low plasma β-parameter in the solar corona. It is therefore interesting to monitor the footpoint motion in order to obtain information on the location and rate of magnetic reconnection. In the standard 2D flare model it is expected that the X-point progressively rises to higher altitudes, and thus consequently the footpoint separation should increase with time. This is observable in some cases, for instance during the Bastille-Day 2000 flare (Fig. 9, bottom frame). However, because large flares always show double ribbons that can have a considerable length along the neutral line, up to 200,000 km (in the Bastille-Day 2000 flare), 3D flare models are required. Magnetic reconnection sometimes progresses along the neutral line ("zipper effect"), and thus the motion of footpoints and coronal hard X-ray sources is observed to move systematically parallel to the ribbons (e.g., Krucker et al. 2003). The motion parallel to the flare ribbons can be so dominant that no perpendicular motion of footpoints is observed at all, which suggests that the reconnection progresses horizontally rather than vertically (Grigis & Benz 2005b).

Based on reconnection models, the energy release rate can be written as the

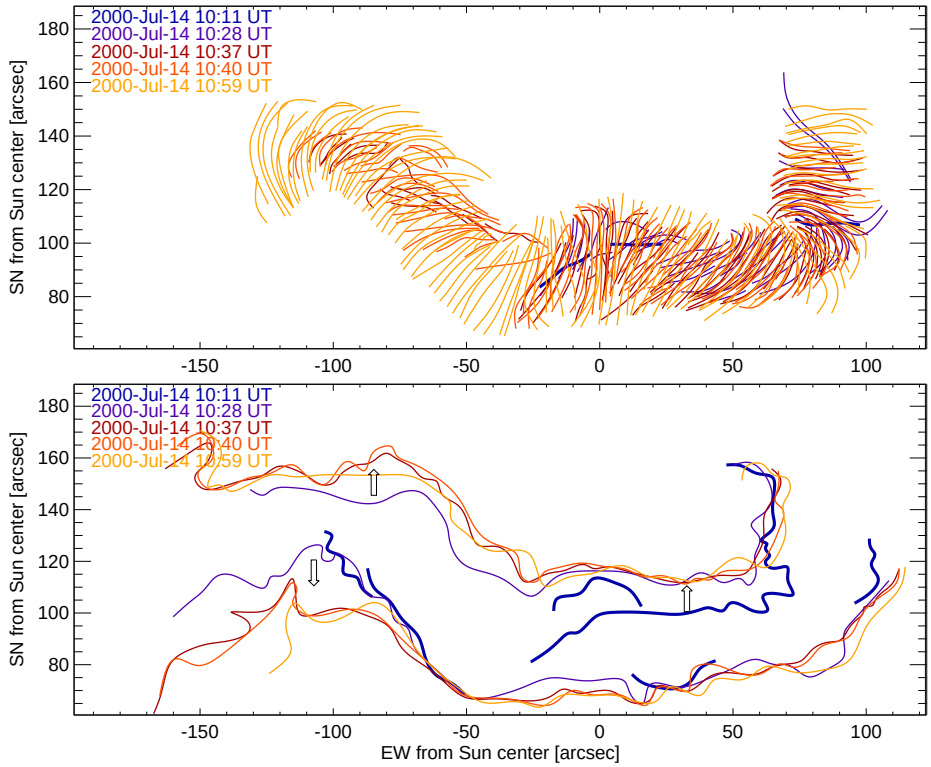

Figure 9. *Top: Tracings of individual flare loops from TRACE 171 Å images of the Bastille-Day flare 2000 July 14, 10:11 UT, rendered with different greytones during 5 subsequent time intervals, evolving from low-lying strongly sheared to high-lying less sheared loops. Bottom: The position of the two flare ribbons are traced from 171 Å images. Note the increasing footpoint separation with time (Aschwanden 2004).*

product of the Poynting flux S into the reconnection region and the area A of the reconnection region,

$$\frac{dW}{dt} = SA = 2\frac{B_c^2}{4\pi} v_i A \; , \tag{1}$$

where B_c is the magnetic field strength in the corona and v_i is the inflow velocity into the reconnection region. Using the flare ribbon motion to estimate the lateral inflow velocity v_i and the extrapolated photospheric magnetic field to estimate the coronal value B_c, an approximate correlation was found between the estimated energy release rate dW/dt and the observed hard X-ray or microwave fluxes (Asai et al. 2004; Jing et al. 2007).

Alternatively, the electric field **E** in a reconnecting current sheet (RCS) can also be expressed by the product of the ribbon expansion velocity **v** and the local vertical magnetic field strength **B** in the footpoint (Forbes & Priest 1984), which

essentially is propotional to the Lorentz force,

$$\mathbf{F} = q\mathbf{E} = \mathbf{j} \times \mathbf{B} = \frac{q}{c} n(\mathbf{v} \times \mathbf{B}) \tag{2}$$

which was used to explain the spatial anticorrelation between the local hard X-ray flux (thought to be proportional to the acceleration rate in the electric field) and the hard X-ray spectral index (which is proportional to the ratio of accelerated high-energy to low-energy electrons), (Liu et al. 2008). Similarly, the Lorentz force drives the shearing motion during magnetic flux emergence, according to recent numerical magnetohydrodynamic (MHD) simulations (Manchester 2007), which may control the acceleration of particles in associated flares, and thus could explain correlations between the hard X-ray flux and the product of the ribbon velocity **v** with the local vertical magnetic field **B**.

3.7 *Footpoint versus Looptop Nonthermal Hard X-ray Emission*

Generally, nonthermal hard X-ray emission is dominantly produced at the footpoints of flare loops, because the density in the acceleration region and along the propagation path to the footpoints is not prohibitivly high to stop the free-streaming precipitating nonthermal electrons. Faint nonthermal coronal hard X-ray sources were only discovered since Masuda et al. (1994). With the high spectral resolution of RHESSI, however, an increasing number of events was detected that had dominant nonthermal emission near the loop top (Fig. 10), rather than at the footpoints (Veronig & Brown 2004). The loop column densities in two cases were found to be sufficiently high to explain the hard X-ray emission in terms of nonthermal thick-target bremsstrahlung in the corona (Veronig & Brown 2004). Similarly high densities ($n_e \approx 10^{10}$ cm^{-3}) of nonthermal electrons in the coronal flare source were also inferred from radio observations (White et al. 2003). The lack of dominant footpoint emission may even indicate that chromospheric evaporation is not primarily driven by precipitating particles, as generally assumed in the standard model, but rather by thermal conduction from the hot loop top (Veronig & Brown 2004).

The nonthermal hard X-ray spectrum of footpoint and loop top sources is also expected to be different. In the simplest theoretical model, one expects that the spectrum at the loop top, dominated by thin-target emission (with a slope of $\gamma_{thin} = \delta + 1$, with δ being the powerlaw slope of the electron injection spectrum), to be steeper than the spectrum at the footpoints, dominated by thick-target emission (with a slope of $\gamma_{thick} = \delta - 1$, by an amount of $\gamma_{thin} - \gamma_{thick} = 2$. However, a RHESSI study of 5 flares with separate spectral fits at loop top and footpoint sources reveals a larger range than theoretically predicted, from $(\gamma_{top} - \gamma_{foot}) \gtrsim 0.6$ to $\lesssim 3.6$ (Battaglia & Benz 2006). Although the observations follow the theoretically expected trend, more detailed modeling of the time-dependent evolution of trapped electron distributions in asymmetric magnetic reconnection geometries is needed to understand the details.

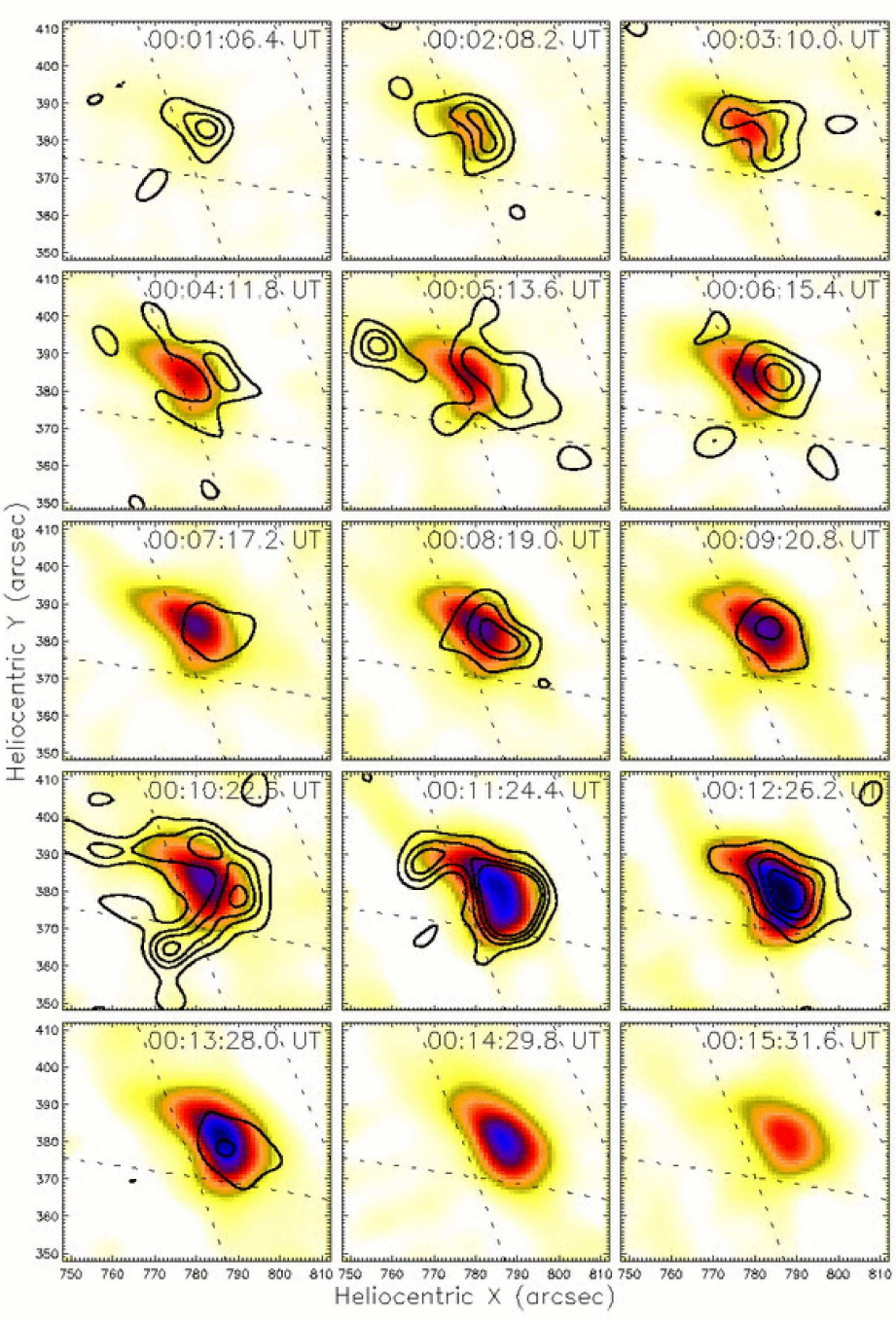

Figure 10. *RHESSI maps in the 6-12 keV energy range are shown for the 2002 April 14, 23:56 UT, flare. The contours indicate the 25-50 keV energy range. Note the almost complete absence of* > 25 *keV nonthermal emission at the footpoints (Veronig & Brown 2004).*

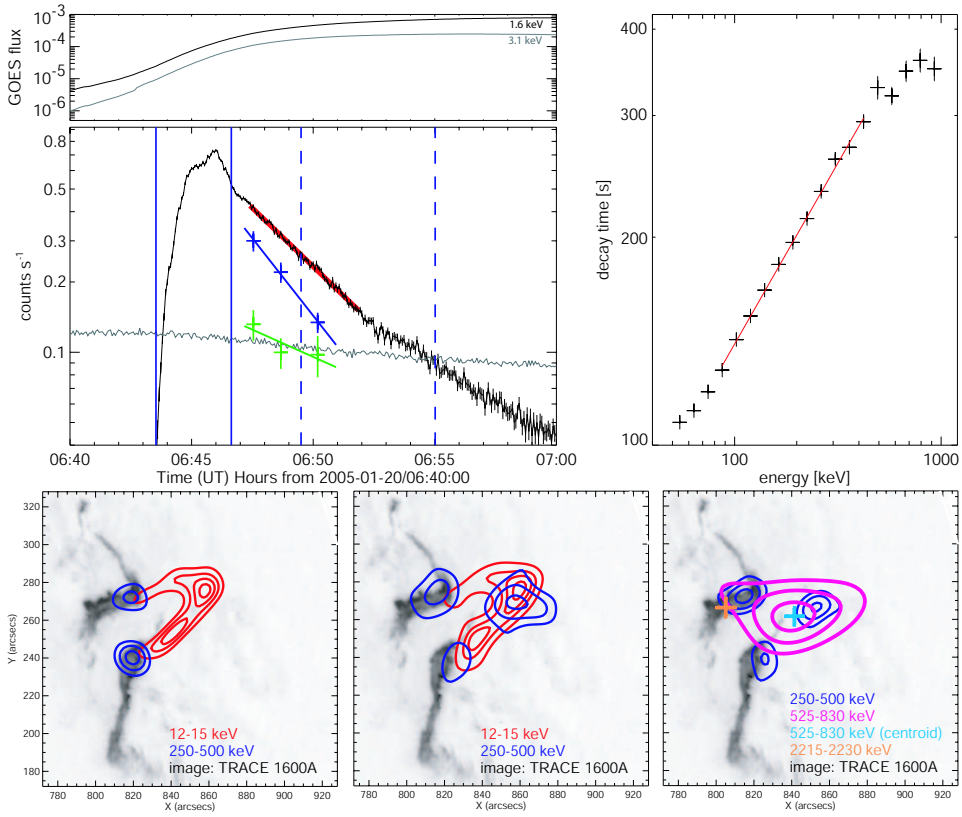

Figure 11. *RHESSI and GOES time profiles of the 2005 Jan 20, 06:40 UT, flare are shown (top left), with the energy-dependence of the fitted exponential decay time (top right), and RHESSI contours in different energy bands overlaid on TRACE images (bottom row). Note the coronal 250-500 keV gamma-ray continuum emission at the loop top later in the flare (Krucker et al. 2008).*

3.8 *Footpoint versus Looptop Gamma-Ray Emission*

Gamma-ray emission is usually expected in the footpoints of flare loops, where the chromospheric density is sufficiently high to produce either gamma-ray line emission (from nuclear deexcitation lines) or gamma-ray continuum emission (from bremsstrahlung of relativistic electrons). RHESSI is the first instrument that allows us to image gamma-ray emission above 100 keV in cases of sufficient photon count statistics. So far, only three events with best counting statistics have been analyzed for coronal emission at the highest energies (Krucker et al. 2008). The analysis of these three events (one is shown in Fig. 11) shows the existence of coronal gamma-ray sources (besides the usual footpoint sources) with very hard spectra (with powerlaw slopes in the range of 1.5-2), suggesting that high-relativistic (> 1 MeV) electrons are trapped in the corona that produce bremsstrahlung in gamma-

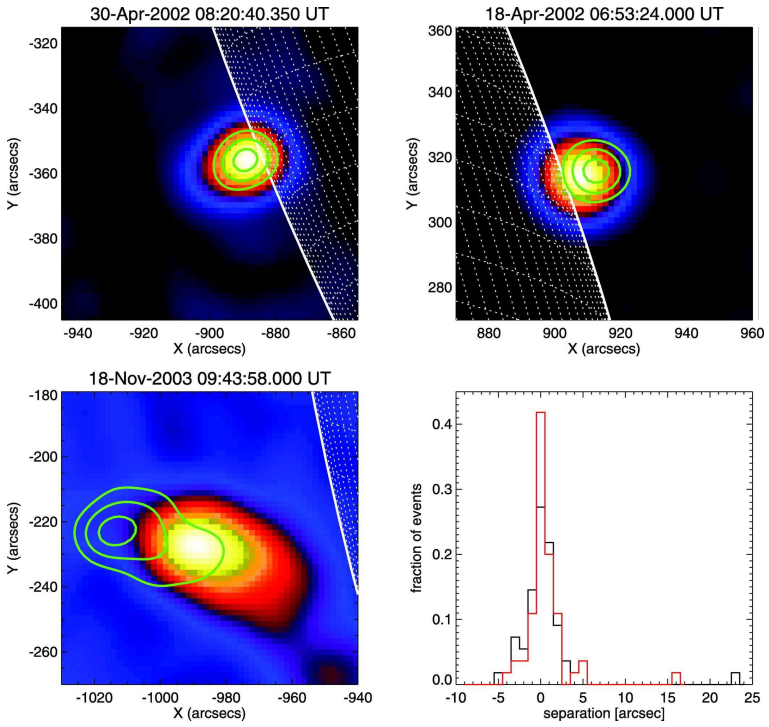

Figure 12. *RHESSI maps of 6-12 keV thermal emission, with overlaid contours of the 20-30 keV nonthermal emission of three occulted flares (2002 Apr 30, 2002 Apr 18, and 2003 Nov 18). The bright nonthermal footpoint sources are occulted. The histogram in the bottom right shows the separation of the centroids between the thermal and nonthermal sources (Krucker & Lin 2008).*

rays. The associated gamma-ray emission exhibits also a strict exponential decay time, as it is common for leaking particle traps. Moreover, the decay time increases with higher energies, as it is expected for collisional traps (where the trapping time is given by the collisional deflection time).

3.9 *Nonthermal Sources in Occulted Flares*

The dominant nonthermal hard X-ray emission is hidden behind the solar limb in occulted flares, so we can potentially detect alternative and weaker nonthermal sources higher up in the corona in the flaring region. In the simplest scenario, electrons and ions are accelerated in the cusp regions of a coronal magnetic reconnection site and stream then down to the flare loop footpoints. As a consequence we expect dominantly nonthermal thick-target bremsstrahlung at the footpoints and thermal emission in the soft X-ray flare loops after they have been filled with heated plasma by chromospheric evaporation. However, low-energy electrons ($\lesssim 15$ keV) are already stopped in the corona on their way down to the footpoints, so that they

produce thin-target as well as thick-target bremsstrahlung in the coronal portions of the flare loops. Even more interestingly, nonthermal emission has also been seen up to $\lesssim 50$ keV in the so-called above-the-loop top sources discovered by Masuda et al. (1994), which requires unusual high electron densities or trapping times significantly longer than the collisional deflection time. Occulted flares can reveal such coronal traps, because the thick-target emission from traps is not outshone by the bright nonthermal footpoint thick-target emission. In fact, initial RHESSI results of 55 partially disk-occulted flares reveal that 90% show not only thermal emission at lower energies but also additional nonthermal emission extending to higher energies with fast time variations and a soft spectrum, see examples in Fig. 12 (Krucker & Lin 2008). It was concluded that the rapidly-varying component is produced by thin-target bremsstrahlung (i.e., faint hard X-ray production without significant collisional energy losses) by the same population of electrons that later precipitate and lose their energy by collisional thick-target emission in loop footpoints (Krucker et al. 2007b; Krucker & Lin 2008).

3.10 *Hard X-ray Emission from the Very High Corona*

If a flare occurs far behind the limb, hard X-ray emission from both the footpoint and loop tops are occulted. The flare of 2002 Oct 27, 22:50 UT was observed on-disk by a *Gamma-Ray Spectrometer (GRS)* orbiting Mars, at an angle of 40° behind the solar limb for RHESSI, but RHESSI detected hard X-ray emission up to 60 keV for this high-occulted flare (Krucker et al. 2007a). The RHESSI-observed hard X-ray source was found to be occulted by at least 200″(or 0.2 solar radius), and the spectrum was found to show a long exponential decay with progressive spectral hardening. Such spectral features are characteristic for coronal traps. This unique observation thus witnesses flare-associated injection of nonthermal electrons into very high coronal traps. Alternatively, hard X-ray emission at such very high coronal altitudes could also be produced in CME shocks, but the outward motion of the hard X-ray source was found to move with approximately the speed of the filament trailing the CME, which is slower than the speed of the CME front. The number of hard X-ray producing electrons in the very high corona was found to be only a small fraction of the total accelerated electrons. The fraction of nonthermal (> 10 keV) electrons in the very high corona was estimated to be about 10%.

3.11 *Hard X-ray Albedo Emission from the Photosphere*

In standard flare models, particles are accelerated near magnetic reconnection regions in the corona, from where they precipitate to the chromosphere to produce the bulk of thick-target bremsstrahlung. The observed hard X-ray emission, however, is a mixture of the primary bremsstrahlung of precipitating electrons and a Compton-backscattered component from the photosphere (Fig. 13). This photospheric albedo component was first detected and studied in solar flares with RHESSI (Kasparova et al. 2005; Kontar et al. 2006, 2007; Schmahl & Hurford 2003) and with Monte-

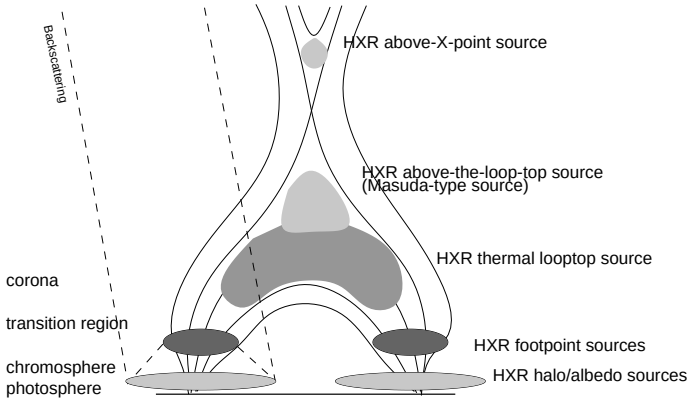

Figure 13. *Schematic overview of physically different hard X-ray sources: thermal hard X-ray source at the flare loop top, nonthermal hard X-ray sources at flare loop footpoints, above the flare loop top (Masuda-type), and above X-point, and hard X-ray albedo sources from backscattering at the photosphere.*

Carlo simulations (Bai & Ramaty 1978). Since the magnitude and angular function of the backscattering radiation depends on the directivity of the impinging particle distribution function, statistical measurements of the photospheric albedo at different line-of-sight angles to the photospheric surface yield essential information on the anisotropy of the precipitating particle distribution and even on their altitude (Bai & Ramaty 1978). The albedo component was found to produce a dip in the mean electron flux distribution $\overline{n}V\overline{F}(E)$ that is fitted to the photon spectrum, which may modify the best spectral fits of a given electron acceleration/propagation model, the inferred lower energy cutoff, total electron number and energy (Kasparova et al. 2005; Kontar et al. 2006, 2007). The albedo is expected to show a strong center-to-limb variation in the 15-20 keV range, which was indeed verified in a statistical analysis (Kasparova et al. 2007). Modeling the hard X-ray spectrum of two flares with two components of downward- and upward-directed electrons, a near-isotropic electron distribution function was found, which contrasts standard thick-target models that include strong downward beaming (Kontar & Brown 2006). Therefore, these measurements are not consistent with the standard thick-target model, unless the electrons are efficiently isotropized before they are collisionally stopped. Although the spectral flattening at low energies can be explained with the albedo-effect of an isotropic electron distribution (Kontar et al. 2006, 2007), it was found to fit the observed spectra of only 3 (out of 9) flares with a spectral flattening at low energies (Sui et al. 2007). The counter-evidence for strongly beamed precipitating particles may also explain the near absence or marginal detection of gamma-ray polarization in the 100-300 keV energy range (Boggs et al. 2006; Suarez-Garcia et al. 2006).

3.12 *Onset of Particle Acceleration in Flares*

The coronal acceleration of electrons to > 10 keV during the rise phase was for the first time clearly demonstrated with RHESSI because previous instruments had insufficient spectral resolution to separate the thermal from the nonthermal spectral component in the $10 - 20$ keV energy range (Lin et al. 2003a, 2003b).

Particle acceleration is expected to occur not before the onset of significant energy release, once magnetic reconnection has started, usually marked with the detectable rise of hard X-rays. Interestingly, microwave emission (at 17 and 34 GHz), an unambiguous signature of gyrosynchrotron emission of high-relativistic electrons, was already detected in the preflare phase (some 10 min) before the onset of hard X-rays, which could flag the build-up of accelerating fields and production of microwave-emitting electrons already before a significant amount of hard X-ray-producing electrons is produced (Asai et al. 2006).

3.13 *Time Evolution of Hard X-ray Spectra*

The overall time evolution of hard X-ray spectra follows generally the soft-hard-soft pattern, or soft-hard-harder pattern, the latter being more likely in large flare events accompanied with interplanetary solar particle events (Kiplinger 1995).

Tracking the spectral evolution with higher time evolution, the spectral soft-hard-soft pattern seems to occur for each subpeak of the impulsive flare phase, as shown for a statistical set of 24 flares observed with RHESSI, and thus seems to be an intrinsic signature of the elementary acceleration process (Grigis & Benz 2004). Modeling the pitch-angle distribution of electrons subjected to a stochastic acceleration process in a leaking trap can reproduce the basic soft-hard-soft spectral evolution, with a pivot point around 10 keV, but a modification of the model with enhanced trapping through an electric potential is necessary to reproduce the observed 20 keV hard X-ray flux (Grigis & Benz 2005a, 2006). Electron trapping times in the order of $\approx 1 - 10$ s were also inferred from energy-dependent time delay fits of hard X-ray subpeaks observed with CGRO (Aschwanden et al. 1997), which is equivalent to a soft-hard spectral evolution during the rise time of each hard X-ray subpeak. The spectral soft-hard evolution could therefore be an universal characteristic of coronal acceleration mechanisms with temporary trapping.

3.14 *CME-Driven Particle Acceleration*

A direct relationship between the CME kinematics and particle acceleration was recently reported by Temmer et al. (2008). The acceleration profile of the CME front was found to be exactly correlated with the RHESSI hard X-ray flux (Fig. 14) in two flares. This closely correlated evolution between both phenomena was interpreted in terms of a feedback relationship between the CME dynamics and the reconnection process in the current sheet beneath the CME. More specifically, the impulsive acceleration phase of the CME and the associated currents are thought

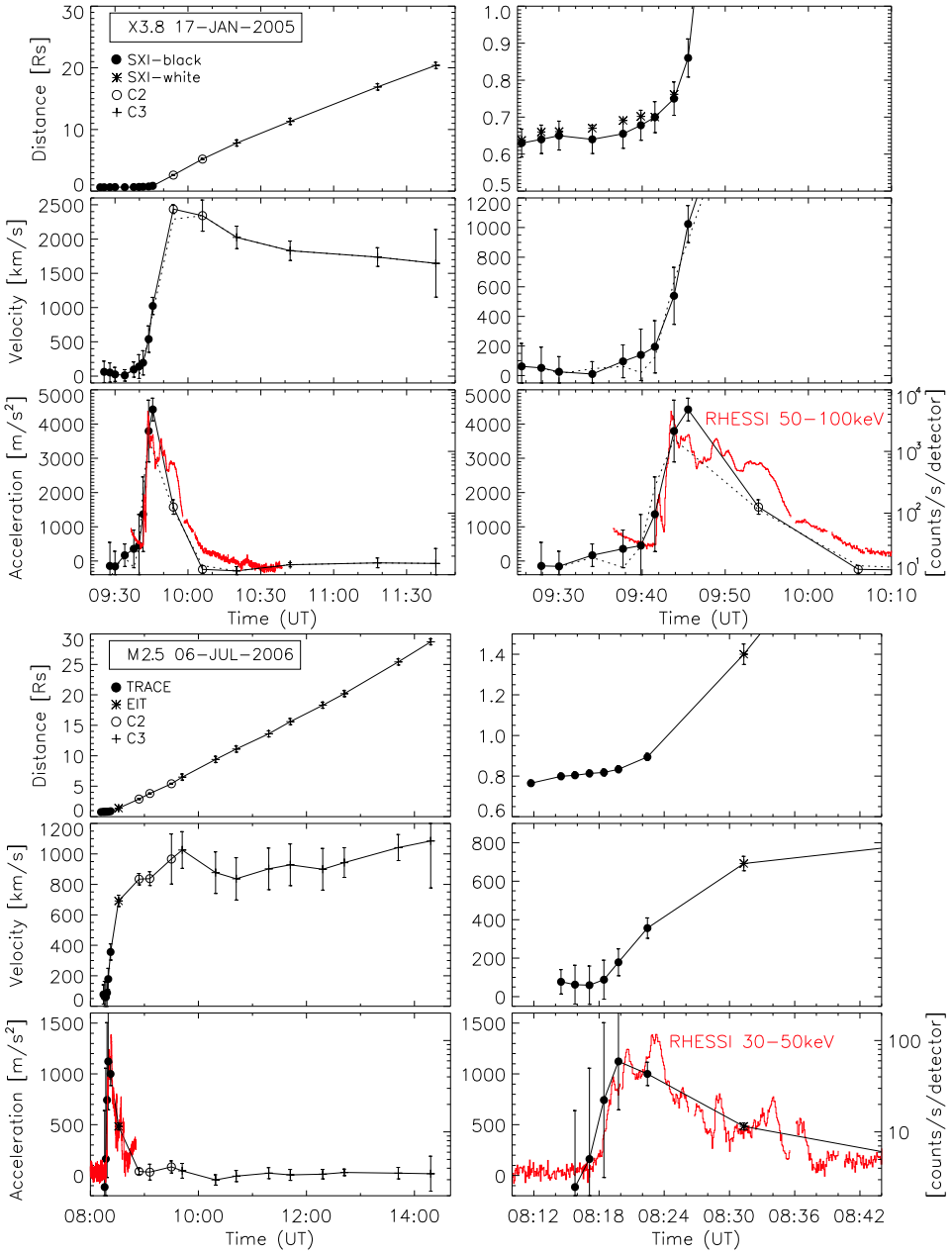

Figure 14. *The flare/CME events of 2005 Jan 17 (top) and 2006 Jul 6 (bottom) are shown in form of height-time, velocity, and acceleration profiles, measured from LASCO. The RHESSI 50-100 keV flux is overlaid on the acceleration profiles. Note the detailed correlation between the CME acceleration profile and the hard X-ray flux (Temmer et al. 2008).*

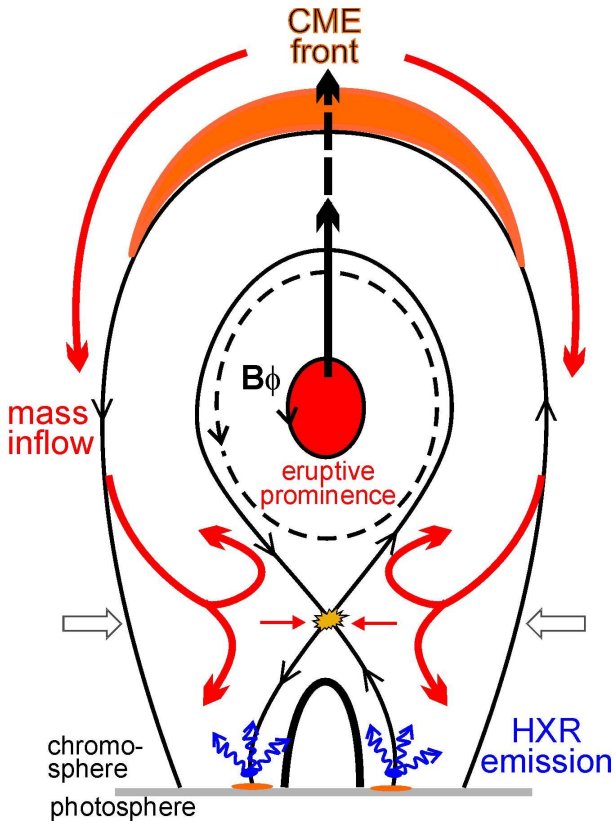

Figure 15. *Cartoon that pictures the feedback mechanism between the mass inflow driven by the CME front motion into the X-point reconnection region, with concomitant particle acceleration and hard X-ray emission (courtesy of Manuela Temmer).*

to be driven by the Lorentz force, as shown in recent MHD simulations of Manchester (2007). The resulting currents control the inflow of new material into the reconnection region in the current sheet beneath the CME, which produces a proportional output of accelerated particles in the reconnection outflow, and this way explains the correlation with the hard X-ray flux (Fig. 15). This is probably the first measurement of a direct connection between the particles *before* and *after* acceleration in solar flares. More detailed modeling of this process could determine the acceleration efficiency and the number problem of accelerated particles.

3.15 *Particle Acceleration and Radio Emission*

While we mostly focused on new RHESSI observations in this review, which observes the hard X-ray emission of energized particles, we neglected the radio counterpart here (for a review see Benz 2008), which also is produced by nonthermal electrons, but the interpretation of the nonlinear radio emission mechanisms

involves generally more unknown parameters than the well-understood free-free bremsstrahlung mechanism in hard X-rays. However, there is a host of recent RHESSI-associated radio observations that shed some light on the process of particle acceleration, such as MHD simulations of radio-emitting electrons accelerated in a reconnection region (Karlicky 2008), or gyrosynchrotron emission at 210 GHz produced by highest-energy particles in the 60-150 MeV range (Trottet et al. 2008), for example.

4. Final Remarks

RHESSI faciliated a lot of unprecedented observations due to its first imaging capability of solar hard X-rays and gamma-rays above 100 keV, as well as due to its high spectral resolution capability. While RHESSI enabled us to observe for the first time new hard X-ray components in solar flares, such as dual loop top sources bracketing the X-point reconnection geometry, coronal gamma-ray emission, or photospheric albedo emission, we are left with a challenging modeling task of the magnetic configuration between the acceleration regions and the hard X-ray producing energy loss sites, in order to learn more quantitative physics about the acceleration process itself and the inseparable particle propagation kinematics. RHESSI enormously improved our spectral modeling capabilities, because the thermal and nonthermal components can now be separated much clearer, but it confronted us also with new spectral modeling problems, related to the photospheric albedo component, partial chromospheric ionization, or instrumental pulse pile-up. The solar limb provides us sometimes a knive's edge to bring out tenuous coronal hard X-ray and gamma-ray sources by occulting the bright footpoints, but we need stereoscopic observations to model the occulted parts at the same time. So, each flare observation brings out different details, while no event shows all aspects simultaneously. How much progress can we assert to the fundamental problem of particle acceleration in solar flares, or astrophysical plasmas in general? Although we gathered a number of unique observations with RHESSI that elucidate individual physical processes, there is still a huge gap between the fundamental theory of particle acceleration in electromagnetic fields and the interpretation of our high-quality RHESSI observations, which can only be filled with detailed hydrodynamic, magnetic, and kinetic modeling.

Acknowledgements: The author gratefully acknowledges input and figures for this review from various RHESSI researchers and from documents of the RHESSI *Heliophysics Senior Review* proposal 2008 to NASA. - This work is partially supported by NASA contract NAS5-98033 of the RHESSI mission through University of California, Berkeley (subcontract SA2241-26308PG), and NASA contract NAS5-38099 for the TRACE mission.

References

Asai, A., Masuda, S., Yokoyama, T., Shimojo,M., Isobe, H., Kurokawa, H., and Shibata, K. 2002, ApJ 578, L91.

Asai, A., Yokoyama, T., Shimojo, M., Masuda, S., Kurokawa, H., & Shibata, K. 2004, ApJ 611, 557.

Asai, A., Nakajima, H., Shimojo, M., White, S.M., Hudson, H.S., & Lin,R.P. 2006, PASJ 58, L1.

Aschwanden, M.J., Bynum, R.M., Kosugi, T., Hudson, H.S., & Schwartz, R.A. 1997, ApJ 487, 936.

Aschwanden, M.J., Kosugi, T., Hanaoka, Y., Nishio, M., & Melrose,D.B. 1999, ApJ 526, 1026.

Aschwanden, M.J. 2002, Space Science Rev. 101, 1.

Aschwanden, M.J., Brown, J. C., & Kontar, E. P. 2002, Solar Phys. 210, 383.

Aschwanden, M.J. 2004 (1st ed.) 2005 (paperback ed.), *Physics of the Solar Corona. An Introduction*, Springer: New York.

Aschwanden, M.J. 2006, Space Science Rev. 124, 361.

Bai, T. & Ramaty, R. 1978, ApJ 219, 705.

Battaglia, M. & Benz, A.O. 2006, AA 456, 751.

Benz, A.O. 1993 (1st ed.), 2002 (2nd ed.), *Plasma Astrophysics: Kinetic Processes in Solar and Stellar Coronae*, Astrophysics and Space Science Library, Vol. 279, Kluwer: Dordrecht.

Benz, A.O. 2008, Living Reviews in Solar Physics, 5, 1.

Boggs, S.E., Coburn, W., & Kalemci, E. 2006, ApJ 638, 1129.

Dennis,B.R., Hudson,H.S., & Krucker,S. 2007, Lecture Notes in Physics, 725, 33.

Emslie, A. G., Miller, J. A., & Brown, J. C. 2004, ApJ 602, L69.

Fletcher, L., Metcalf, T. R., Alexander, D., Ryder, L. A., & Brown, D. S. 2001, ApJ 554, 451.

Forbes, T.G. & Priest, E.R. 1984, SP 94, 135.

Grigis, P. C. & Benz, A. O. 2004, AA 426, 1093.

Grigis, P. C. & Benz, A. O. 2005a, AA 434, 1173.

Grigis, P. C. & Benz, A. O. 2005b, ApJ 625, L143.

Grigis, P. C. & Benz, A. O. 2006, AA 458, 641.

Hanaoka, Y. 1996, SP 165, 275.

Heyvaerts, J., Priest, E.R., & Rust,D.M. 1977, ApJ 216, 123.

Holman, G.D., Aschwanden, M.J., Aurass, H., Battaglia, M., Grigis, P.C., Kontar, E.P., Liu, W., Saint-Hilaire, P., & Zharkova,V.V. 2008, SSRv (subm.).

Hurford, G. J., Schwartz, R. A., Krucker, S., Lin, R. P., Smith, D. M., & Vilmer, N. 2003, ApJ, L77.

Hurford, G. J., Krucker, S., Lin, R. P., Schwartz, R. A., Share, G. H., & Smith, D. M. 2006, ApJ 644, L93.

Jain, R. & 14 co-authors, 2005, Solar Phys. 227, 89.

Jing, J., Lee, J., Liu, C., Gary, D. E., & Wang, H. 2007, ApJ 664, L127.

Karlicky, M., Veronig, A., & Vrsnak, B. 2006, Central Europ. Astroph. Bull. 30, 85.
Karlicky, M. 2008, AJP, p... (in this volume).
Kasparova, J., Karlicky, M., Kontar, E.P., Schwartz, R.A., & Dennis,B.R. 2005, SP 232, 63.
Kasparova, J., Kontar, E.P., & Brown, J.C. 2007, A&A 466, 705.
Kiplinger, A.L. 1995, ApJ 453, 973.
Kontar, E.P., MacKinnon, A.L., Schwartz, R.A. & Brown J.C., 2006, A&A 446, 1157.
Kontar, E.P. & Brown,J.C. 2006, ApJ 653, L149.
Kontar, E.P., Emslie, A.G., Massone, A.M., Piana, M., Brown, J.C., & Prato, M. 2007, ApJ 670, 857.
Krucker, S., Hurford, G. J., & Lin, R. P. 2003, ApJ 595, L103.
Krucker, S. & Hudson, H. S. 2004, in Proc. of SOHO-15 Workshop on "Coronal Heating", ESA SP-575, 247.
Krucker, S., White, S.M., & Lin, R.P. 2007a, ApJ 669, L49.
Krucker, S., Hannah, L.G., & Lin, R.P. 2007b, ApJ 671, L193.
Krucker, S. & Lin, R.P. 2008, ApJ 673, 1181.
Krucker, S., Hurford, G.J., MacKinnon, A.L., Shih, A.Y., and Lin, R.P. 2008, ApJ 678, L63.
Lin, R. P. & 65 co-authors, 2002, Solar Phys. 210, 3.
Lin, R. P. & 12 co-authors, 2003a, ApJ 595, L69.
Lin, R.P., Krucker, S., Holman, G.D., Sui, L., Hurford, G.J., & Schwartz, R.A., 2003b, in Proc. 28th Int. Cosmic Ray Conference, (eds. Kajita, T. et al.), Universal Academy Press, Inc., 6, 3207.
Liu, C., Lee, J.W., Gary, D.E., & Wang,H. 2007a, ApJ 658, L127.
Liu, C., Lee, J.W., Yurchyshyn, V., Deng, N., Cho, K.S., Karlicky, M., & Wang, H. 2007b, ApJ 669, 1372.
Liu, C., Lee, J.W., Gary, D.E., & Wang, H. 2008, ApJ 672, L69.
Liu, W., Liu, S., Jiang, Y.W., & Petrosian, V. 2006, ApJ 649, 1124.
Manchester, W. IV. 2007, ApJ 666, 532.
Masuda, S., Kosugi, T., Hara, H., Tsuneta, S., & Ogawara,Y. 1994, Nature 371, 495.
Melrose, D.B. 1997, ApJ 486, 521.
Moore, R.L., Sterling, A.C., Hudson, H.S., & Lemen, J.R. 2001, ApJ 552, 833.
Nishio, M., Yaji, K., Kosugi, T., Nakajima, H., Sakurai, T. 1997, ApJ 489, 976.
Schmahl, E.J. & Hurford, G.J. 2003, AdSpR 32, 2477.
Shibata, K., Ishido, Y., Acton, L.W., Strong, K.T., Hirayama, T., Uchida, Y., McAllister, A.H., Matsumoto, R., Tsuneta, S., Shimizu, T., Hara, H., Sakurai, T., Ichimoto, K., Nishino, Y., & Ogawara, Y. 1992, PASJ 44, L173.
Suarez-Garcia, E., Hajdas, W., Wigger, C., Arzner, K., Guedel,M., Zehnder,A., & Grigis, P. 2006, SP 239, 149.
Sui, L. & Holman, G.D. 2003, ApJ 596, L251.
Sui, L., Holman, G.D., & Dennis, B.R. 2006, ApJ 645, L157.

Sui, L., Holman, G.D., & Dennis, B.R. 2007, ApJ 670, 862.
Temmer, M., Veronig, A.M., Vrsnak, B., Rybak, J., Gomory, P., Stoiser, S., Maricic, D. 2008, ApJ 673, L95.
Trottet, G., Krucker, S., Luthi, T., & Magun, A. 2008, ApJ 678, 509.
Tsuneta, S., Hara, H., Shimizu, T., Acton, L.W., Strong, K.T., Hudson, H.S., & Ogawara,Y. 1992, PASJ 44, L63.
Veronig, A.M. & Brown, J.C. 2004, ApJ 603, L117.
Vestrand, W.T. & Forrest, D.J. 1993, ApJ 409, L69.
White, S.M., Krucker, S., Shibasaki, K., Yokoyama, T., Shimojo, M., & Kundu, M.R. 2003, ApJ 595, L111.
Zharkova, V.V. & Gordovskyy, M. 2004, ApJ 604, 884.